Electronic Supplementary Material (ESI) for Physical Chemistry Chemical Physics.
This journal is © the Owner Societies 2014

Double-QM/MM Method for Investigating Donor–Acceptor Electron Transfer Reactions in Solution

Zdenek Futera,[a,b,c] Keitaro Sodeyama,[b,d] Jaroslav V. Burda[e] Yasuaki Einaga[a,c] and Yoshitaka Tateyama*[b,c,d,f]

[a] *Keio University, 3-14-1 Hiyoshi, Kohoku-ku, Yokohama 223-8522, Japan*
[b] *International Center for Materials Nanoarchitectonics (WPI-MANA), National Institute for Materials Science (NIMS), 1-1 Namiki, Tsukuba, Ibaraki 305-0044, Japan. E-mail: TATEYAMA.Yoshitaka@nims.go.jp*
[c] *CREST, Japan Science and Technology Agency (JST), 4-1-8 Honcho, Kawaguchi, Saitama 333-0012, Japan*
[d] *Elements Strategy Initiative for Catalysts and Batteries, Kyoto University, Goryo-Ohara, Kyoto 615-8245, Japan*
[e] *Department of Chemical Physics and Optics, Faculty of Mathematics and Physics, Charles University, Ke Karlovu 3, 121 16 Prague 2, Czech Republic*
[f] *PRESTO, Japan Science and Technology Agency (JST), 4-1-8 Honcho, Kawaguchi, Saitama 333-0012, Japan*

Contents

S1 Program QMS **S1**
S1.1 Program Structure S1
S1.2 Parallelization S1
S1.3 Charge Embedding S2
S1.4 Computational Methods S2

S2 Hexaaqua $Fe^{2+/3+}$ and $Ru^{2+/3+}$ Complexes **S3**
S2.1 QM Models S3
S2.2 QM/MM Models S3
S2.3 Explicit vs. Implicit Solvent S4
S2.4 Ionization Energies S4
S2.5 Dependence on DFT functionals and atomic pseudopotentials S5

S1 Program QMS

Multiple–QM/MM method (*m*-QM/MM) described in the article was implemented in a new software called QMS. To obtain flexible program that can exploit well tested MM potentials and variety of QM methods available in standalone software, we designed QMS as an interface capable to couple these MM and QM programs and perform combined QM/MM calculations. In current version, Amber MM program package[49] can be linked with the QM software Gaussian[48], GAMESS[S1], MolPro[S2] or Turbomole[S3].

S1.1 Program Structure

The QMS program is a package of three main binary modules and several small additional scripts, which interface the communication with the external QM and MM software (see the scheme in Fig. S1). The first module, *QMS*–Prep, is an interactive program that helps user to partition the system and prepare all necessary input files for the QM/MM calculation. The calculation itself is performed by the *QMS*–Step module, the core part of the QMS package. The program can evaluate energy of a particular system structure, minimize the total energy of the system with respect to atomic coordinates or run Born–Oppenheimer molecular dynamics (BOMD) under specified conditions. The calculated trajectory can be analyzed by the last *QMS*–Prep module.

S1.2 Parallelization

In order to increase efficiency of the QM/MM calculations, evaluation of the QM electron densities of inner parts is done simultaneously with the MM calculations (Fig. S2). POSIX Thread library[S4] is employed to create new thread for each part of the system when the external programs are called. Because the evaluation of the MM energies proceeds much faster than the QM calculation, the MM contributions are treated by the master thread in series. Most of the QM software can perform the calculation of the electronic properties on more than one CPU to speed up the SCF iterative cycle. This capability is exploited in the QMS program as a second level of the parallelization.

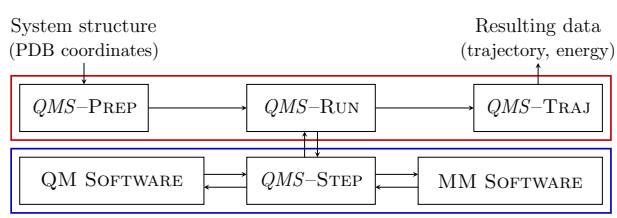

Fig. S1 Schematic structure of the QMS program package and data flow between its modules. The red frame indicates user interface while the blue frame shows an internal part of the program.

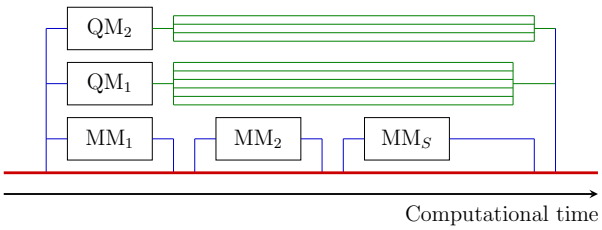

Fig. S2 Schematic illustration of *QMS*–Step module parallelization. Master thread (red) calls QM and MM programs, gathers data from all parts and compile them. QM calculation of each inner part can be further parallelized by external software (green, 4 CPUs and 6 CPUs per 1 QM part in this example).

S1.3 Charge Embedding

Two methods how to treat the electrostatic interaction between the inner and outer part, E^{ee}_{I-O}, are implemented in the QMS program; the so–called mechanical embedding, which is implicitly involved in the subtractive QM/MM computational scheme, and a more accurate electrostatic embedding.

Mechanical Embedding In the mechanical embedding, no special treatment of the electrostatic interaction is done, the equations (2), (3) and (4) in the main text are used as they are, and the E^{ee}_{I-O} contribution is fully included in the $E_{\mathrm{MM}}(S)$ term. The E^{ee}_{I-O} contribution is calculated according to the classical Coulomb law:

$$E^{ee-m.e.}_{I-O} = \sum_{A=1}^{N_O} \sum_{B=1}^{N_{I+L}} \frac{Z_A Z_B}{|\mathbf{R}_A - \mathbf{R}_B|} \tag{S1}$$

as an interaction of the atomic point charges, which are defined in the force field. Since the QMS program does not update the point charges on the inner part atoms during the geometry optimization or MD, the charges are kept fixed as they were assigned to the atoms at the beginning of the calculation. Although the mechanical embedding is straightforward and easy to use, the QM electron density of inner part does not reflect its charge environment and can not respond to it by the polarization. Therefore the second approach, electrostatic embedding, is more often used.

Electrostatic Embedding In the electrostatic embedding, the atomic point charges from the outer part are included in the QM Hamiltonian of the inner part

$$E^{ee-e.e.}_{I-O} = \sum_{A=1}^{N_I} \int_V \frac{Z_A \rho(\mathbf{r})}{|\mathbf{R}_A - \mathbf{r}|} d\mathbf{r} \tag{S2}$$

The charge density $\rho(\mathbf{r})$ adapts to the electrostatic field of the MM charges Z_A during the SCF cycle and as a result the electron density becomes polarized.

However, it is not computationally efficient to include all the MM charges into the QM Hamiltonian if the supercell is large. Therefore, a charge layer (CL) of the MM atoms around each inner part can be defined in the QMS program and only the atoms from this layer are used in the electrostatic embedding (see Figure 1b in the main text). In such case, the $E^{ee-e.e.}_{I-CL}$ contribution is included in the $E_{\mathrm{QM}}(I)$ term of Eq. 2 but the whole $E^{ee-e.e.}_{I-O}$ remains in the $E_{\mathrm{MM}}(S)$ after subtraction of $E_{\mathrm{MM}}(I)$. To avoid double–counting, the $E^{ee-e.e.}_{I-CL}$ contribution evaluated at the MM level must be subtracted from the total $E_{\mathrm{MM}}(S)$ as well. This problem is, in current version of the QMS program, solved by four different evaluations of the MM energy of the whole system S per one QM calculation:

1. Charges on all the S atoms are defined.
2. Charges on the I atoms are the same as in the case 1; charges on the O atoms are set to 0.
3. Charges on the CL atoms are the same as in the case 1, charges on the I atoms and those from the $O \notin CL$ are set to 0.
4. Charges on the $I + CL$ atoms are the same as in the case 1, charges on the I atoms and those from the $O \notin CL$ are set to 0.

and finally the electrostatic contribution from the outer part calculated at the MM level is

$$\begin{aligned} E^{ee-e.e.}_{\mathrm{MM}}(S) = & E^{ee-e.e.}_{\mathrm{MM}}(S)[1] - E^{ee-e.e.}_{\mathrm{MM}}(S)[2] - \\ & - \left\{ E^{ee-e.e.}_{\mathrm{MM}}(S)[4] - E^{ee-e.e.}_{\mathrm{MM}}(S)[2] - \right. \\ & \left. - E^{ee-e.e.}_{\mathrm{MM}}(S)[3] \right\} = \\ = & E^{ee-e.e.}_{\mathrm{MM}}(S)[1] - E^{ee-e.e.}_{\mathrm{MM}}(S)[4] + \\ & + E^{ee-e.e.}_{\mathrm{MM}}(S)[3] \end{aligned} \tag{S3}$$

where numbers in square brackets denote different charge assignment defined above. All terms in Eq. S3 are evaluated by Ewald summation when periodic boundary conditions are used.

S1.4 Computational Methods

Besides the total QM/MM energy evaluation, the geometry optimization or BOMD can be performed by the QMS program. Three different optimization algorithms are available in the code: steepest descent, conjugate gradients with Fletcher–Reeves[S5], Polak–Ribière[S6] or Hestenes–Stiefel[S7] conjugation factor and limited memory Broyden–Fletcher–Goldfarb–Shanno (L-BFGS) method[S8]. Regarding BOMD, velocity Verlet algorihm[S9] was implemented together with Andersen[S10] and Berendsen[S11] thermostat for NVT ensemble simulations. Because the QM/MM calculations are computational demanding, all these methods do not use higher order derivatives of total energy than its gradient.

This journal is ©The Royal Society of Chemistry [2014]

Complex / 2S+1		1	3	5
$[Fe(H_2O)_6]^{2+}$	GP	+1.46	+1.31	0.00
	PCM	+1.20	+1.17	0.00
$[Ru(H_2O)_6]^{2+}$	GP	0.00	+0.34	+0.82
	PCM	0.00	+0.93	+1.22

Complex / 2S+1		2	4	6
$[Fe(H_2O)_6]^{3+}$	GP	+1.48	+1.29	0.00
	PCM	+0.83	+0.89	0.00
$[Ru(H_2O)_6]^{3+}$	GP	0.00	+0.98	+1.28
	PCM	0.00	+1.26	+2.13

Table S1 Differences of the total energies of $[M(H_2O)_6]^{2+/3+}$ (M = Fe, Ru) complexes [eV] for different spin–states. The energy values are relative with respect to the most stable complex in gas phase (GP) and implicit solvent (PCM), evaluated at B3LYP/6-31++G(d,p) level with SDD pseudopotentials on M centers.

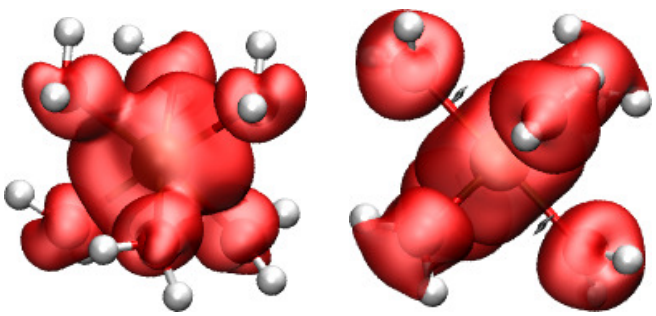

$[Fe(H_2O)_6]^{2+}$, $2S+1=5$ $[Fe(H_2O)_6]^{3+}$, $2S+1=6$

Fig. S3 Spin densities $\rho_\uparrow(\mathbf{r})-\rho_\downarrow(\mathbf{r})$ on $[Fe(H_2O)_6]^{2/3+}$ high spin–state complexes evaluated at B3LYP/6-31G(d) level with SDD pseudopotential on iron.

S2 Hexaaqua $Fe^{2+/3+}$ and $Ru^{2+/3+}$ Complexes

S2.1 QM Models

To create computational models for *s*-QM/MM and *d*-QM/MM calculations we first optimized geometries of $[Fe(H_2O)_6]^{2/3+}$ and $[Ru(H_2O)_6]^{2/3+}$ complexes at the QM level and checked their spin-state stabilities. From data summarized in Table S1 it is obvious that while the Ru complexes are more stable in low–spin–state configuration, the high–spin–state electron arrangement is more stable in Fe complexes.

All the complexes have octahedral structures that is for $[Fe(H_2O)_6]^{2+}$ and $[Ru(H_2O)_6]^{3+}$ slightly elongated in one direction as a result of Jahn–Teller effect. Average M–O bond lengths (M = Fe, Ru) in the optimized structures in their most stable spin–states are listed in Table S2.

The optimized geometries in gas phase were used for the calculation of atomic charges needed for the MM parametrization of the complexes. The electron density was recalculated on the fixed structures at HF/6-31G(d) level and the electrostatic potential was evaluated on grid points selected according to Merz–Singh–Kollman scheme[S12,S13]. Finally, the atomic charges were fitted by RESP method[46,47] and their values are summarized in Table S3. The charges evaluated by this procedure are compatible with Amber[49] force fields and TIP3P water model[41].

All the QM calculations were performed by the program Gaussian 09[48], and charge fitting was done by program RESP that is part of AmberTools program package[49].

S2.2 QM/MM Models

To check consistency of the *d*-QM/MM results with *s*-QM/MM in dilute limit, both single and double component models were created. In the single component cases, structure of each optimized complex was parametrized by GAFF[45] with calculated RESP charges, put into the virtual box together with chloride counterions and the box was then filled by 3325 TIP3P[S14] water molecules. Size of the rectangular box is the same for all cations, 49.706 × 49.684 × 49.327 Å, obtained by preliminary calculations at room temperature. Then, the two–stage equilibration heating to room temperature T = 298.15 K was performed. First, 10 ps MD run with time step Δt = 1.0 fs was performed by Amber with constrained geometries of the metals and their first hydration shells and then the 5 ps QM/MM MD run with time step Δt = 0.5 fs was done on the whole unconstrained system using the QMS program. The QM inner parts of the system were treated at B3LYP/6-31G(d) level with Stuttgart–Dresden (SDD) pseudopotentials[42–44] on the metal atoms, charge and spin–state was kept fixed at desired value for each inner part.

The two component systems were created analogically. Donor–acceptor pairs, Fe^{2+} + Ru^{3+} resp. Fe^{3+} + Ru^{2+} hexaaqua–complexes, were put into the 76.203 × 54.296 × 57.630 Å simulation box together with five chloride counterions and surrounded by 6470 TIP3P water molecules. At the

Bond	QM_{GP}	QM_{PCM}	QM/MM
Fe^{2+}–O	2.163	2.153	2.158
Fe^{3+}–O	2.055	2.028	2.030
Ru^{2+}–O	2.146	2.139	2.143
Ru^{3+}–O	2.077	2.060	2.065

Table S2 M–OH_2 distances [Å] calculated at B3LYP/6-31G(d) level with SDD pseudopotential[42–44] on metal centers. QM data are measured on the optimized structures in the gas phase (GP) or in C-PCM while the QM/MM data are averages from the 950 MD samples.

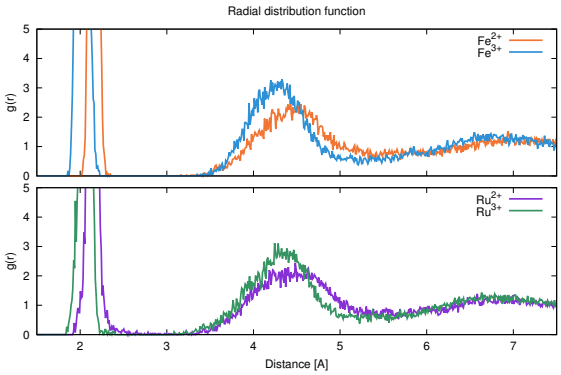

Fig. S4 Radial distribution function of the M–O bond lengths evaluated from QM/MM MD trajectory. The trajectory was calculated at B3LYP/6-31G(d) level of QM parts with SDD pseudopotentials on metal centers. MM water was parametrized by TIP3P model.

		QM_{GP}	QM_{PCM}	*s*-QM/MM
Fe^{2+}	ΔE	17.16	6.83	8.76
Fe^{3+}	ΔE	16.28	5.80	3.73
Ru^{2+}	ΔE	16.27	5.79	7.82
Ru^{3+}	ΔE	15.45	5.00	3.04
$Fe^{2+/3+}$	ΔA	16.72	6.32	6.25
	λ	0.44	0.52	2.51
$Ru^{2+/3+}$	ΔA	15.86	5.40	5.43
	λ	0.41	0.40	2.39
Full	ΔA	-0.86	-0.95	-0.81
	λ	0.85	0.91	4.90

Table S4 Comparison of the QM calculations in gas phase (GP) and C-PCM with *s*-QM/MM. All the values were obtained on the optimized structures. The electrostatic embedding was employed in the QM/MM calculations.

beginning, mutual distance of the metal centers was set to 20.0 Å and the box was heated by the procedure described above. Positions of the metal cations were harmonically restrained during this phase. Then, an additional pulling force was applied on each metal in the M–M direction to reach mutual distance R_{DA} = 6.0 Å during following 20 ps QM/MM MD run. The distance range from 6.0 to 20.0 Å was divided into 30 windows, one representative structure was selected for each window and used as an initial geometry for the final productive 20 ps QM/MM MD run with restrained position of metal centers.

Qualitatively correct behavior of the system during MD was checked by radial distribution functions detecting the interaction of the metal centers with the solvent molecules (see Fig. S4). The first sharp peak corresponds to position of oxygens of nearest six water molecules forming the first hydration shell of the cations. These peaks are localized at distances listed in the last column of Table S2. The second peak, although broader than the first one, is still well localized and it detects the average position of water molecules in the second hydration shell that interacts with the hexaaqua complexes via hydrogen bonding. Above ca. 6 Å apart from the metal centers the water distribution becomes to be homogeneous.

Complex	M	O	H
$[Fe(H_2O)_6]^{2+}$	1.395	-0.919	0.510
$[Fe(H_2O)_6]^{3+}$	2.527	-1.143	0.611
$[Ru(H_2O)_6]^{2+}$	0.901	-0.769	0.476
$[Ru(H_2O)_6]^{3+}$	1.235	-0.775	0.535
TIP3P water		-0.834	0.417

Table S3 RESP atomic charges [*e*] calculated at HF/6-31G(d) level with SDD pseudopotential[42–44] on the metal centers M. For comparison, charges on TIP3P water are shown as well.

S2.3 Explicit vs. Implicit Solvent

To stress importance of the explicit treatment of the water solution, we calculated the redox free energy and the reorganization free energy in half–reaction approach at QM level with implicit solvent model (C-PCM) and compared it with the *s*-QM/MM results. These calculations were done on the fully optimized structures and resulting values of the ionization potentials are shown in Table S4. It can be seen that the solvation energy is larger on 3+ complexes in QM/MM than in PCM while the opposite effect can be observed on 2+ complexes. This is caused by the well–known fact that PCM simulates averaged electrostatic field of given environment that is acting on the complexes. The dipole interaction of the water molecules and hydrogen bonding can not be described in the PCM model. A more accurate description is provided by the QM/MM technique where the charge densities of the complexes are polarized by the solvent through electrostatic embedding. As a result, the QM/MM model with the explicit solvent access information about the total reorganization free energy while the QM model can explore only its inner part, λ_{in}. The redox free energy, which is determined by electronic states of the metallic centers is the same in both models because these states are influenced mainly by their first hydration shells.

S2.4 Ionization Energies

To compare *s*-QM/MM with our *d*-QM/MM method in dilute limit (R_{DA} = 20 Å), we evaluated the ionization energies and electron affinities of the metal complexes in both methods and used them for the calculation of the redox free energy and

This journal is ©The Royal Society of Chemistry [2014]

PES		s-QM/MM	d-QM/MM
Fe^{2+}	ΔE	17.07	17.05
Fe^{3+}	ΔE	16.22	16.23
Ru^{2+}	ΔE	16.15	15.96
Ru^{3+}	ΔE	15.46	15.39
$Fe^{2+/3+}$	ΔA	16.64	16.64
	λ	0.43	0.41
$Ru^{2+/3+}$	ΔA	15.80	15.68
	λ	0.35	0.29
Full	ΔA	-0.84	-0.96
	λ	0.77	0.70
	$\Delta A^{\ddagger}$	0.00	0.03

Table S5 Comparison of the half reaction ionization potential and the electron affinities obtained from the QM inner part energies using s-QM/MM and d-QM/MM method, both in mechanical embedding. Metal cations were in dilute limit separation R_{DA} = 20 Å.

PES		s-QM/MM	d-QM/MM$_{half}$	d-QM/MM$_{full}$
Fe^{2+}	ΔE	8.85	8.60	6.72
Fe^{3+}	ΔE	3.95	3.59	2.65
Ru^{2+}	ΔE	8.11	7.45	5.51
Ru^{3+}	ΔE	3.33	2.98	1.47
$Fe^{2+/3+}$	ΔA	6.40	6.09	4.69
	λ	2.45	2.51	2.04
$Ru^{2+/3+}$	ΔA	5.72	5.21	3.49
	λ	2.39	2.24	2.02
Full	ΔA	-0.68	-0.88	-1.20
	λ	4.83	4.74	4.06
	$\Delta A^{\ddagger}$	0.89	0.79	0.50

Table S6 Comparison of the half reaction ionization potential and the electron affinities obtained from the QM inner part energies using s-QM/MM and d-QM/MM method, both in electrostatic embedding. Half–reaction as well as full–reaction scheme d-QM/MM results are listed in the table. Metal cations were in dilute limit separation R_{DA} = 20 Å.

the reorganization free energy. In these calculations, only the QM inner part energies were used, which is the easiest way how to apply the half–reaction computational approach in d-QM/MM. The data are summarized in Table S5 and Table S6 where these two methods are compared both in the mechanical embedding and in the electrostatic embedding. All the values were obtained on the fully optimized geometries as in the previous section.

S2.5 Dependence on DFT functionals and atomic pseudopotentials

All quantities presented in this paper were obtained with DFT(B3LYP) description of the QM inner parts where SDD pseudopotentials and pseudobasis were used on the metal cations. However, choice of the exchange–correlation treatment of the inner parts certainly influences value of the redox free energy, inner part contribution of the reorganization free energy as well as the electronic coupling. Therefore, the appropriate DFT functional or ab–initio method, pseudopotentials and basis set has to be carefully chosen when quantitatively accurate calculations are required.

Here, we demonstrate the dependence of redox free energy ΔA of Fe^{3+} + Ru^{2+} $\rightarrow$ Fe^{2+} + Ru^{3+} ET reaction on the DFT functional and metal pseudopotential. Before examining the overall effect by full d-QM/MM MD simulations, we first calculated the redox free energies of the $[M(H_2O)_6]^{2+}$ $\rightarrow$ $[M(H_2O)_6]^{3+}$ + e (M = Fe, Ru) half–reactions at QM (C-PCM) level. Double–ζ 6-31G(d) basis was used on the aqua–ligand atoms and the free energy corrections to the total energies were evaluated from the vibrational analysis. We combined BLYP[15,16], PBE[17], B3LYP[15,16,18], B3PW91[15,18–20], HSE06[21], LC-BLYP[15,16,22], M06L[23] and wB97XD[24] DFT functionals with SDD[25–27], SBKJC[28], LANL2DZ[29–31], LANL08[29–32] and CRENBL[33] metal pseudopotentials and pseudobasis to calculate the half–reaction redox free energies. These are plotted in Fig. S5.

It can be seen that in the chosen C-PCM model and the relatively small basis set, all the functionals overestimate the experimental half–reaction redox free energies of the Fe and Ru hexaaqua complexes that are 5.21 eV and 4.67 eV, respectively. While the pure GGA functionals (BLYP and PBE) yield values about 0.5 eV above the experimental one, hybrid functionals (B3LYP, B3PW91, HSE06) provide even higher redox free energies. The long–range–corrected LC–BLYP and wB97XD behave similarly to the hybrid functionals while the meta–GGA M06L functional does not differ much from pure GGA results in this case.

However, if the errors included in the half–reaction redox free energies are of the same magnitudes, they cancel in the total full–reaction redox free energy ΔA. The experimental value of ΔA, 0.54 eV, is indicated by the dashed black line in Fig. S5. From the lower panel of the figure it is obvious that the error balance is dependent on the pseudopotential and pseudobasis used for the metal core and valence electrons, respectively. While the popular LANL2DZ and SDD pseudopotentials, which we applied in this work, have a tendency to overestimate ΔA of the Fe^{3+} + Ru^{2+} $\rightarrow$ Fe^{2+} + Ru^{3+} ET reaction, the opposite trend can be seen in case of the SBKJC pseudopotentials. The most balanced half–reaction redox free energies that yield the accurate ΔA with error less than 0.2 eV can be in this particular case obtained with LANL08 pseudopotentials.

Generally, the long–range corrected functionals are sup-

	B3LYP SDD	B3LYP LANL08	LC-BLYP LANL08	wB97XD LANL08
ΔA	0.878	0.722	0.649	0.562
λ	2.593	2.574	2.828	2.671
λ_{in}	0.720	0.725	0.811	0.792
λ_{out}	1.873	1.849	2.017	1.879
$\tilde{\lambda}$	1.756	1.747	1.927	1.831
$\Delta\tilde{A}^{\ddagger}$	0.110	0.150	0.212	0.220
V_{DA}	0.020	0.011	0.263	0.014
$\tilde{k}_{DA}$	$2.14 \cdot 10^{+1}$	$4.32 \cdot 10^{0}$	$4.57 \cdot 10^{-1}$	$3.05 \cdot 10^{-1}$

Table S7 Comparison of the MD sampling results for the touching–part limit of the full–reaction with three different exchange–correlation treatments of the QM inner parts. The quantities where the empirically rescaled λ was used are marked by tilded symbols.

posed to provide better description of the charge density at one–electron level[34] Therefore we can expect that these functionals might yield the more accurate value of the electronic coupling that we evaluated at the two–state approximation in this work. To show the overall effect of the exchange–correlation treatment, we performed the full–reaction MD simulations at touching–part limit with the LC–BLYP and wB97XD functionals combined with LANL08 pseudopotentials. For comparison, the B3LYP functional with the LANL08 was checked as well. Indeed, the LC–BLYP gives V_{DA} higher by one order comparing with the B3LYP case, as it can be seen from the results collected in Table S7, whereas practically unchanged value was obtained by wB97XD. As expected, both long–range–corrected functionals improve the value of the total redox free energy. However, the reorganization free energy slightly increases, which leads to higher free energy barrier of the reaction. Because the barrier enters the exponential Franck–Condon factor of the rate constant, this effect is dominant and the rate constant decreases by two orders.

References for Supporting Information

1 M. W. Schmidt, K. K. Baldridge, J. A. Boatz, S. T. Elbert, M. S. Gordon, J. H. Jensen, S. Koseki, N. Matsunaga, K. A. Nguyen, S. Su, T. L. Windus, M. Dupuis and M. J. A., *J. Comput. Chem.*, 1993, **14**, 1347–1363.

2 H.-J. Werner, P. J. Knowles, R. Lindh, F. R. Manby, M. Schütz, P. Celani, T. Korona, A. Mitrushenkov, G. Rauhut, T. B. Adler, R. D. Amos, A. Bernhardsson, A. Berning, D. L. Cooper, M. J. O. Deegan, A. J. Dobbyn, F. Eckert, E. Goll, C. Hampel, G. Hetzer, T. Hrenar, G. Knizia, C. Köppl, Y. Liu, A. W. Lloyd, R. A. Mata, A. J. May, S. J. McNicholas, W. Meyer, M. E. Mura, A. Nicklass, P. Palmieri, K. Pflüger, R. Pitzer, M. Reiher, U. Schumann, H. Stoll, A. J. Stone, R. Tarroni, T. Thorsteinsson, M. Wang and A. Wolf, *Molpro, version 2006.1, a package of ab initio programs*, 2006.

3 R. Ahlrichs, M. Bär, M. Häser, H. Horn and C. Kölmel, *Chem. Phys. Lett.*, 1989, **162**, 165.

4 *POSIX.1c, Threads extensions (IEEE Std 1003.1c-1995).*

5 R. Fletcher and C. M. Reeves, *Comp. J.*, 1964, **7**, 149–154.

6 B. Polak and G. Ribiere, *Rev. Fr. Imform. Rech. Oper.*, 1969, **16**, 35–43.

7 M. R. Hestenes and E. Stiefel, *J. Res. Nat. Bur. Std.*, 1952, **49**, 409–436.

8 D. C. Liu and J. Nocedal, *Math. Program.*, 1989, **45**, 503–528.

9 W. C. Swope, C. Andersen, P. H. Berens and K. R. Wilson, *J. Chem. Phys.*, 1982, **76**, 637.

10 H. C. Andersen, *J. Chem. Phys.*, 1980, **72**, 2384–2393.

11 H. J. C. Berendsen, J. P. M. Postma, W. F. van Gunsteren, A. DiNola and J. R. Haak, *J. Chem. Phys.*, 1984, **81**, 3684–3690.

12 U. C. Singh and P. A. Kollman, *J. Comp. Chem.*, 1984, **5**, 129–145.

13 B. H. Besler, K. M. J. Merz and P. A. Kollman, *J. Comp. Chem.*, 1990, **11**, 431–439.

14 W. L. Jorgensen, J. Chandrasekhar, J. D. Madura, R. W. Impey and M. L. Klein, *J. Chem. Phys.*, 1983, **79**, 926–935.

15 A. D. Becke, *Phys. Rev. A*, 1988, **38**, 3098–3100.

16 C. Lee, W. Yang and R. G. Parr, *Phys. Rev. B*, 1988, **37**, 785–789.

17 J. P. Perdew, K. Burke and M. Ernzerhof, *Phys. Rev. Lett.*, 1996, **77**, 3865–3868.

18 A. D. Becke, *J. Chem. Phys.*, 1993, **98**, 5648–5652.

19 J. P. Perdew, J. A. Chevary, S. H. Vosko, K. A. Jackson, M. R. Pederson, D. J. Singh and C. Fiolhais, *Phys. Rev. B*, 1992, **46**, 6671–6687.

20 J. P. Perdew, K. Burke and Y. Wang, *Phys. Rev. B*, 1996, **54**, 16533–16539.

21 J. J. Heyd and G. E. Scuseria, *J. Chem. Phys.*, 2004, **121**, 1187–1192.

22 H. Iikura, T. Tsuneda, T. Yanai and K. Hirao, *J. Chem. Phys.*, 2001, **115**, 3540–3544.

23 Y. Zhao and D. G. Truhlar, *J. Chem. Phys.*, 2006, **125**, 194101.

24 J.-D. Chai and M. Head-Gordon, *Phys. Chem. Chem. Phys.*, 2008, **10**, 6615–6620.

25 D. Andrae, U. Häussermann, M. Dolg, H. Stoll and H. Preuß, *Theor. Chim. Acta*, 1990, **77**, 123–14.

26 D. Andrae, U. Häussermann, M. Dolg, H. Stoll and H. Preuß, *Theor. Chim. Acta*, 1991, **78**, 247–266.

27 A. Bergner, M. Dolg, W. Kuechle, H. Stoll and H. Preuss, *Mol. Phys.*, 1993, **80**, 1431.

28 W. J. Stevens, M. Krauss, H. Basch and P. G. Jasien, *Can. J. Chem.*, 1992, **70**, 612–630.

29 P. J. Hay and W. R. Wadt, *J. Chem. Phys.*, 1985, **82**, 270–283.

30 W. R. Wadt and P. J. Hay, *J. Chem. Phys.*, 1985, **82**, 284–298.

31 P. J. Hay and W. R. Wadt, *J. Chem. Phys.*, 1985, **82**, 299–310.

32 L. E. Roy, P. J. Hay and R. L. Martin, *J. Chem. Theory Comput.*, 2008, **4**, 1029–1031.

33 M. M. Hurley, L. F. Pacios, P. A. Christiansen, R. B. Ross and W. C. Ermler, *J. Chem. Phys.*, 1986, **84**, 6840–6853.

34 T. Stein, H. Eisenberg, L. Kronik and R. Baer, *Phys. Rev. Lett.*, 2010, **105**, 266802.

This journal is ©The Royal Society of Chemistry [2014]

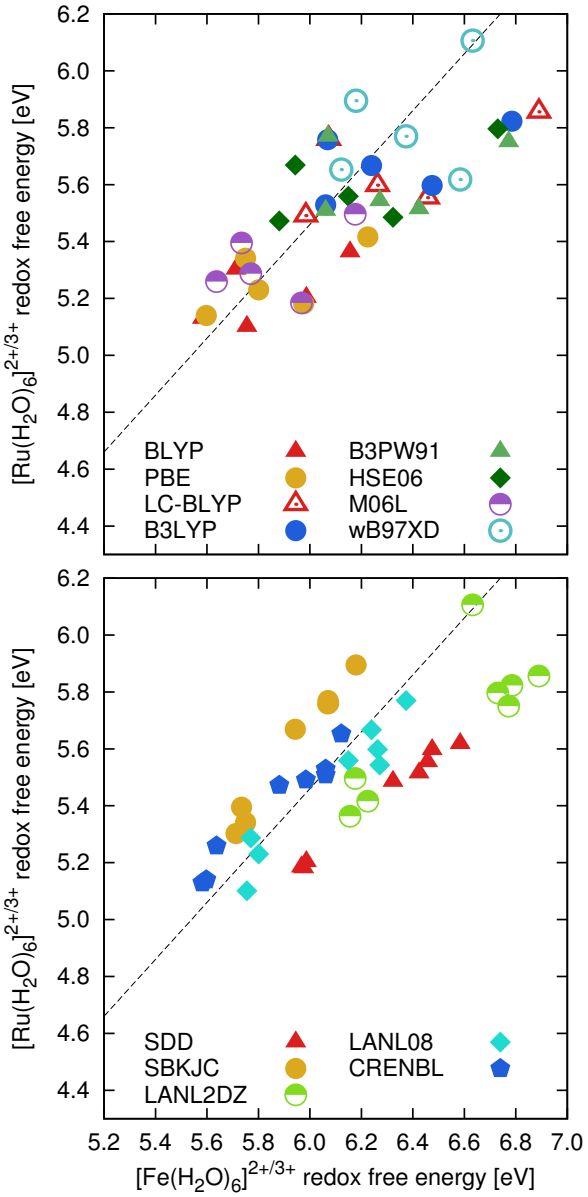

Fig. S5 DFT functional dependence (upper panel) and pseudopotential dependence (lower panel) of half–reaction redox free energies of $[Fe(H_2O)_6]^{2+/3+}$ and $[Ru(H_2O)_6]^{2+/3+}$ complexes. The values were obtained at QM (C-PCM) level with 6-31G(d) basis set on aqua ligand atoms. The dashed black line indicates the experimental full–reaction redox free energy 0.54 eV.